Transient large strain contact modelling: A comparison of contact techniques for simultaneous fluid–structure interaction

Espino, Daniel M.; Shepherd, Duncan E.t.; Hukins, David W.l.

DOI:
10.1016/j.euromechflu.2015.01.006

Accepted Manuscript

Transient large strain contact modelling: A comparison of contact techniques for simultaneous fluid-structure interaction

Daniel M. Espino, Duncan E.T. Shepherd, David W.L. Hukins

PII: S0997-7546(15)00016-3
DOI: http://dx.doi.org/10.1016/j.euromechflu.2015.01.006
Reference: EJMFLU 2861

To appear in: *European Journal of Mechanics B/Fluids*

Received date: 22 February 2013
Revised date: 20 January 2015
Accepted date: 20 January 2015

Please cite this article as: D.M. Espino, D.E.T. Shepherd, D.W.L. Hukins, Transient large strain contact modelling: A comparison of contact techniques for simultaneous fluid-structure interaction, *European Journal of Mechanics B/Fluids* (2015), http://dx.doi.org/10.1016/j.euromechflu.2015.01.006

HIGHLIGHTS

- A true-transient contact modelling method for FSI simulations is presented.
- Transient FSI contact modelling is necessary to predict fluid dynamics.
- Transient FSI modelling is necessary to predict structural deformation.

Transient large strain contact modelling: a comparison of contact techniques for simultaneous fluid-structure interaction.

Daniel M Espino*, Duncan ET Shepherd & David WL Hukins

School of Mechanical Engineering, University of Birmingham, Birmingham, UK B15 2TT

*Corresponding author:

Daniel Espino

School of Mechanical Engineering,

University of Birmingham,

Birmingham,

UK

B15 2TT

e-mail: daniel.m.espino@gmail.com

tel. +44 (0) 121 414 7355

fax. +44 (0) 121 414 3958

ABSTRACT

Contact between two deformable structures, driven by applied fluid-pressure, is compared for an existing pseudo-transient contact method (the default in the Comsol Multi-physics v3.3 software package) and a new transient method. Application of the new method enables time-dependant and simultaneous Fluid Structure Interaction (FSI) simulations to be solved. The new method is based on Hertzian contact. It enables truly transient simulations, unlike the default contact method. Both the default and new methods were implemented using a moving Arbitrary-Lagrange Euler mesh, along with velocity constraints and Lagrange Multipliers to enable simultaneous FSI simulations. The comparison was based on a simple two-dimensional model developed to help understand the opening of a heart valve. The results from the new method were consistent with the steady-state solutions achieved using the default contact method. However, some minor differences in fluid dynamics, structural deformation and contact pressure predicted were obtained. The new contact method developed for FSI simulations enables transient analysis, in contrast to the default contact method that enables steady state solutions only.

KEY WORDS: Fluid Structure Interaction, Hertzian contact, Large strain, Multi-physics modelling.

1. Introduction

The aim of this study was to test a new transient two-dimensional contact method in a simultaneous Fluid-Structure Interaction (FSI) simulation. This contact method has been used with Comsol Multi-physics (v3.3, Comsol Ltd, London) to test its application for FSI simulations. The simplifying assumption made was that negligible translation occurred between opposing contacting boundaries. All other contact conditions remained unchanged.

We have previously discussed the limitations of the default contact modelling method using Comsol multi-physics [1,2]; the key limitation is poor transient implementation. Such limitations meant our initial simultaneous FSI simulations of the mitral heart valve only simulated inflow and ignored valve contact [3]. Subsequently the FSI mitral heart valve model was assessed following implementation of the developed transient contact method [4]. However, assessment of its application to simultaneous FSI modelling is currently limited to that mitral heart valve model. A more generic assessment is necessary to enable its application more widely. There are potential applications to other recently developed FSI heart valve models [5] and to articular cartilage, found at the end of bones in joints such as the hip and knee, where load bearing and hydration are important to its mechanics [6]. For example, there is evidence that replacement materials for articular cartilage which mimic its physical behaviour are advantageous [7], with biphasic models often used to study how cartilage on cartilage contact induces flow of the underlying fluid [8]. Beyond the biomedical field, micro-electro-mechanical-systems often use cantilevers which are deformed through fluid flow [9], leading to potential applications in models with which to study their application for

say nanotribology [10]. Hence, a generic description enables the study of FSI which involves contact modelling to be extended beyond the assumption of a rigid contacting surface [11].

In this paper, our new contact method is compared with the existing (default) contact method under FSI conditions, where hydrodynamic fluid flow induces contact by inducing large strain in the structure. Solutions for fluid and structure response were calculated simultaneously for each time step, i.e. 'true' multi-physics simulations were performed, as opposed to one-way or iterative coupling of physical states [12]. The Comsol Multi-physics package was used for this study as it allows simultaneous coupling of distinct physical states, as in FSI. Therefore, it is not necessary to iterate between Finite Element (FE) and Computational Fluid Dynamics (CFD) simulation software.

Simultaneous FSI simulations use Lagrange multipliers for non-ideal weak-form constraints, equivalent to the reaction forces on boundaries shared by a structure and fluid [13-15]. During FE analysis Lagrange multipliers enforce constraints; for simultaneous FSI simulations the Lagrange multipliers are also used to determine reaction forces [13-15]. The velocity of the moving structure provides a boundary condition for the fluid velocity at the boundary between the structure and fluid [13-15]. The mesh used for calculating fluid hydrodynamics is typically fixed to the original geometry (using an Eulerian method), but the mesh to determine structural deformation usually follows the deforming shape of the structure (it uses a Lagrangian method). In order to couple the two meshes, an Arbitrary-Lagrange-Euler (ALE) mesh is used [16-17]. A standard ALE mesh is not recommended for large strain modelling; hence, a moving ALE mesh

approach has been used which removes the need for computationally expensive remeshing [18].

This new transient contact method is based on Hertzian contact. It has been developed for two-dimensional large-strain conditions, roughly replicating those relevant to heart valve closure. Therefore, structure and fluid properties used in this study resemble those of heart valves and blood. However, this contact method is generic and, thus, applicable to other FSI simulations where contact modelling is important.

2. Methods

2.1 Overview

A new transient FSI contact method and the default contact method available in the software [19] were compared. Contact simulations were simultaneous, transient multi-physics models, with the force that induces contact being applied by fluid flow and pressure. The default contact method solves steady-state solutions for the conditions at the stated time-step.

2.2 Geometry

Two identical conduits were set beside one another with two deformable structures (termed anterior and posterior valve leaflets, because of the intended application to heart valves) attached to their larger facing side (figure 1). The two leaflets were the only deformable structures; thus, only leaflets could come into contact. The leaflet geometry used is identical to that used for a static FE analysis described previously [1]. These leaflets correspond, roughly, to the two contacting leaflets of the mitral valve of the heart (a valve that closes due to contact between the two leaflets). The conduits in which fluid flows do not resemble the heart, but they do allow fluid flow to induce leaflet deformation, inducing contact, so allowing an FSI contact simulation. Further detail on the anatomy of the mitral valve and left ventricle is available elsewhere [20].

2.3 Material properties

Material properties of structures and fluid were selected to resemble those of heart valve leaflets and blood (table 1). The fluid was assumed incompressible (i.e. constant density)

and Newtonian (i.e. constant viscosity). Blood is a non-Newtonian fluid; however, the approximation of being Newtonian is suitable for large scale flow [21] as occurs in this simulation. The leaflets were assumed isotropic and linearly elastic [1].

2.4 Boundary conditions

Fluid boundary conditions included (figure 1): the two shorter sides of each conduit that served to define the outflow (defined by equation 1, the fluid velocity vector, with equation 2 defining the velocity time-dependency) and time-dependent pressure, P (equation 3), respectively. In order to mimic a non-zero initial pressure on the structure, a starting pressure of 100 Pa was applied. All other boundaries in the fluid domain, with the exception of those shared with the structure (i.e. belonging to the leaflets), were given a no-slip condition (equation 4). Shared boundaries were given an inflow-outflow condition (equation 1) but with the velocity of flow being equivalent to the velocity of the moving structure (equation 5). The total time (T) for the simulation was 10 s.

$$\vec{u} = u\hat{i} + v\hat{j} \qquad 1$$

$$u = 0, \qquad v = v_p\left(t/T\right) \qquad 2$$

$$P = P_p\left(t/T\right) + 100 \qquad 3$$

$$\vec{u} = 0 \qquad 4$$

$$u = \delta x/\delta t, \qquad v = \delta y/\delta t \qquad 5$$

Where P_p, $\vec{u}$, u, v, and v_p, refer to the peak pressure, velocity vector, initial velocity components along the *x*-and *y-axes* and peak *y-axis* velocity component, respectively.

Note, $\hat{i}$, $\hat{j}$, and $\hat{k}$ are three mutually perpendicular vectors that define a right-handed Cartesian coordinate system. Time is denoted by t.

For *structural boundaries,* shorter edges of the rectangle were restricted from moving (figure 1). The only loading applied was that of fluid pressure on the boundary shared by the leaflet structure and fluid domains. The loading was applied by the fluid on the shared fluid-structure boundary. Contact was applied between the two contacting structure only boundaries. For the new contact method, the contact force at each node, B (equation 6; i.e. Hertzian contact) was applied assuming negligible translation tangential to the contact surface.

$$B = \begin{cases} \tau - gC, g < 0 \\ \tau e^{-g\left(C/\tau\right)}, g \geq 0 \end{cases} \qquad 6$$

Here C is a large constant (1×10^9) and τ is an approximation of the contact force. g is the gap between contacting boundaries (calculated between opposing nodes of the two contact boundaries, using a linear transformation with the boundary extrusion variable function to share position/displacement values between the nodes to calculate the gap).

For *ALE boundaries,* a moving ALE mesh was applied where structure (i.e. any geometry) and fluid were in contact to one another at that boundary [18]. With the exception of such boundaries on the leaflets, all boundaries were set to no mesh displacement. However, leaflet boundaries that were shared (by fluid and structure) were set to have a displacement equivalent to the corresponding structural displacement (equations 1 and 5).

In the fluid domain, a free displacement condition was used for the ALE mesh; while in the solid domain a physics-induced displacement condition was implemented.

This constrains the movement/deformation of the ALE mesh, over the leaflet (i.e. solid domain), to the calculated leaflet movement/deformation. The fluid domain ALE mesh was allowed free displacement. Thus, mesh deformation/displacement is only limited by surrounding geometrical mesh boundaries. Use of either Neumann (i.e. specifying the value of the derivative of the solution) or Dirichlet (i.e. specifying the value of the solution) boundary conditions [22-23] was pre-determined for the partial differential equations by the software. For this study these default boundary conditions were not altered.

2.5 Fluid domain

Simulations of fluid mechanics (i.e. CFD) were solved using the continuity and incompressible Navier-Stokes equations (equations 7 and 8, respectively). The former ensures mass conservation, and the latter momentum balance [23-24].

$$\nabla \cdot \vec{u} = 0 \qquad 7$$

$$\rho \partial \vec{u} / \partial t - \mu \nabla^2 \vec{u} + \rho(\vec{u} \cdot \nabla)\vec{u} + \nabla P = \vec{F} \qquad 8$$

Here, ρ, μ, $\vec{u}$, P, and $\vec{F}$ refer to the density, viscosity, velocity vector field, pressure, and volume force field (i.e. body force) respectively.

The fluid domain was modelled using a weak formulation, under non-ideal conditions [14-15,22,25]. The weak formulation uses Lagrange multipliers and enables accurate transient determination of flux across a boundary [22]. For FSI applications this means reaction forces can be calculated (as equal and opposite to Lagrange multipliers) and used to load a structure, enabling time-dependent and simultaneous solutions. Further details on this method, used for FSI, are available elsewhere [13-15,17,22]. The full

stress tensor was used during calculations, and a corner smoothing method was applied [26]. Corner smoothing improves predicted flow around corners. A stabilisation method of anisotropic streamline diffusion was used. This stabilises the calculated results without the need for mesh refinement. Streamline diffusion applies this method only along streamlines (i.e. anisotropic application parallel but not perpendicular to the streamlines). A tuning parameter of 0.25 was used for the streamline diffusion as recommended for second order element types [27] as used in this study (table 2). Note, the triangular elements used in this study were second order elements and thus had nodes at triangle midpoints and corners [23].

2.6 Fluid-Structure coupling

Fluid and structure interaction required simultaneous, two-way, coupling of shared fluid and deformable solid boundaries (sections 2.4 and 2.5). Briefly, on shared boundaries, the fluid domain provided a loading condition to the structure; while, structural deformation provided a velocity constraint to the fluid.

2.7 Mesh

A moving mesh was utilised without re-meshing (see *ALE boundaries* in section 2.4). ALE mesh domain parameters were solved under non-ideal weak constraints and using Winslow smoothing [28]. A ‘normal’ mesh setting was applied to all simulations (table 2). Further mesh refinement was applied at FSI boundaries (figure 1).

2.8 Solver Settings

A direct UMFPACK solver was used as a non-linear solver is required with the incompressible Navier-Stokes equation [24]. Further details on non-linear and time-dependent solvers are available elsewhere [25]. The solver settings applied in this study are defined elsewhere [1].

A total of 11 variables were solved for each node in FSI simulations using the new contact method, and 12 for those using the default contact method, including:

- solid domain: displacement in the *x-axis* (δx) and *y-axis* δy), which are two orthogonal axes (defining a two dimensional Cartesian coordinate system, see figure 1), and a contact variable solved when using the default contact method;
- fluid domain: pressure (P), velocity in the *x-axis* (u) and *y-axis* (v) directions, and two Lagrange multipliers, one per orthogonal axis, to determine reaction forces on structures (λ_5, and λ_6 corresponding to the *x-* and *y-axis*, respectively);
- ALE-mesh domain: displacement of the mesh in the *x-axis* (δx_{ALE}) and *y-axis* (δy_{ALE}) directions, to enable the moving mesh to follow the deforming structure, and two Lagrange multipliers (λ_3 & λ_4) which were not used for further calculations but are determined as part of a weak formulation.

Simulations were performed on two personal computers: one with 8 GB of RAM and a 64 bit AMD dual-core processor, the other one with 8 GB of RAM and a single core 32 bit Intel processor. Simulations required up to 8 hours for solutions.

3. Results

Both contact methods predicted similar trends for flow patterns, deformations, shear-stress patterns and peak-stress locations (figure 2, & tables 3 & 4). Similar time-dependent trends were also observed with an increase in von Mises and Cauchy stresses, as well as Green strains, contact pressures which were ultimately driven by a rise in the applied time dependent pressure (table 3). Likewise, the magnitude of the velocity field increased, and its components increased with time (table 4). Both models predict asymmetric deformation of the two leaflets (figure 2), in part a result of different mechanical properties (table 1).

There are noticeable differences in predictions, despite general trends being consistent across both contact methods. For example, the new contact method predicted a higher peak contact pressure, over a larger portion of the leaflets at each time step (figure 3). This is consistent with contact occurring earlier with the new contact method (compare figure 2a and 2b). After 10 s, the new contact method predicted 29 kPa of contact pressure as compared to the 25 kPa predicted by the default contact method (table 3). However, an intriguing finding is the prediction of a negative contact pressure by the default contact method for all minimum values, as high as -1.3 kPa at 10 s. This appears to be a numerical artefact of the Hertzian contact model (equation 6), which was not evident for the new contact method developed.

Higher Cauchy stresses and Green strains were generally predicted by the default contact method. However, greater von Mises stresses were predicted after 10 s, with the new contact method leading to predictions of 6.5 MPa, as compared to predictions of 1.1 MPa with the default contact method (table 3). However, development of the stress is

clearly not dependent only on the pressure in the fluid, as higher von Mises stresses were predicted at some earlier time-steps when using the default contact method.

The variation in method predicting the highest von Mises stresses may be a result of differences in predicted fluid flow on the structural boundary which induced its deformation. For example, the Lagrange multiplier which corresponds to *y*-axis reaction forces was greater when using the default contact method (table 4). However, after 10 s the Lagrange multiplier which corresponds to *x*-axis reaction forces was greater for the new contact method (table 4). These differences were reflected in differences in values for vorticity, $\vec{\omega}$ (table 4). Note, vorticity, $\vec{\omega}$, is defined as the curl of the velocity field [25], which in two dimensions can be defined by equation 9 [29].

$$\vec{\omega} = \left(\partial v / \partial x - \partial u / \partial y \right) \hat{k} \qquad 9$$

Greater vorticity predicted by the default contact method could be a consequence of more unsteady flow predicted when using the default contact method (compare figures 2c, and 2e to 2d and 2f). This is supported by higher cell Reynold's numbers calculated when using the default contact method (table 3).

4. Discussion

The new contact method enables use of contact modelling with true-transient analyses, which is of particular benefit for simultaneous FSI simulations where real transient analysis may be important for flow domain solutions. Different peak-values were predicted between default and new contact methods. As the default contact method does not implement a real transient solution, but separate steady state solutions for each time-step, this is not unexpected. However, the stress-patterns predicted were consistent. The new contact method can be quickly implemented if contact occurs with little (or no) translation parallel to the contacting boundary surface; using a standard multi-physics package (Comsol multi-physics v3.3).

The new contact method was developed to overcome limitations with the implementation of the existing contact method for application to heart valves. The main limitation of the existing method was the simplified transient analysis imposed. This was considered inappropriate for future application to simulate mitral heart valves through FSI. Iterative approaches, for example, often led to instabilities in solutions to FSI studies [30-31]. Thus mathematical/numerical approaches such as the fictitious domain [32-33] and immersed boundary [34] FSI methods were developed to enable simultaneous FSI solutions. A steady-state approach or analysis which is not truly transient, therefore, may not be suitable for heart valve modelling of biological valves.

Our FSI simulations do show alterations, particularly in terms of vortices predicted and fluid-loading parameters on the shared fluid-solid boundary. Earlier contact was predicted using the new contact method, which suggests that a converged ‘steady state’ solution for each time-step does not necessarily represent the actual condition

reached through true transient modelling. A curious prediction when using the default contact method was that of negative contact pressures (as high as -1.3 kPa). Presumably, this is a numerical artefact which occurs to ensure convergence of all parameters at each time-step, as solutions are not truly transient. Thus, such a numerical artefacts were not evident when using the new contact method developed, solved transiently. Interestingly, flow profiles appeared to be less turbulent with the new contact method. Again, it is possible that numerical artefacts during convergence also artificially increase the predicted turbulence.

The contact method, used in an FSI simulation, is to be implemented for future studies of heart valve closure. We have previously validated the corresponding valve opening model with experimental results [3]. We plan to further validate our future models using results from our previous studies on mitral valves and their failure [35-36].

ACKNOWLEDGEMENTS

The authors thank the British Heart Foundation for a Junior Fellowship (FS/05/32) awarded to DME during the early part of this investigation. The research leading to these results has received funding from the [European Community's] Seventh Framework Programme [FP7/2007-2013] under a Marie Curie Intra-European Fellowship for Career Development, grant agreement n° [252278], awarded to DME. The funding sources had no involvement in study design; in the collection, analysis and interpretation of data; in the writing of the report; and in the decision to submit the article for publication.

References

[1] D.M. Espino, D.E.T. Shepherd, D.W.L. Hukins, Development of a transient large strain contact method for biological heart valve simulations, Comput. Methods Biomech. Biomed. Engin. 16 (2013) 413-424.

[2] D.M. Espino, D.E.T. Shepherd, D.W.L. Hukins, A simple method for contact modelling in an arbitrary frame of reference within multi-physics software, J. Mech. 29 (2013) N9-N14.

[3] M. Al-Atabi, D.M. Espino, D.W.L. Hukins, Computer and experimental modelling of blood flow through the mitral valve of the heart, J. Biomech. Sci. Eng. 5 (2010) 78-84.

[4] D.M. Espino, D.E.T. Shepherd, D.W.L. Hukins. 2013, Evaluation of a transient, simultaneous, Arbitrary Lagrange Euler based multi-physics method for simulating the mitral heart valve, Comput. Methods Biomech. Biomed. Engin. 17 (2014) 450-458.

[5] K. Hassani, H.R. Bahraseman, M. Navidbakhsh, D.M. Espino, Z. Alizade-Sani, N. Fatouraee, Effect of exercise on blood flow through the aortic valve: a combined clinical and numerical study, Comput. Methods Biomech. Biomed. Engin. 17 (2014) 1821-1834.

[6] B. Pearson, D.M. Espino, Effect of hydration on the frequency-dependent viscoelastic properties of articular cartilage, Proc. Inst. Mech. Eng. H, 227 (2013) 1246-1252.

[7] E. Northwood, J. Fisher, A multi-directional in vitro investigation into friction, damage and wear of innovative chondroplasty materials against articular cartilage, Clin. Biomech., 22 (2007) 834-842.

[8] A.H. Doulabi, K. Mequanint, H. Mohammadi, Blends and nanocomposite biomaterials for articular cartilage tissue engineering, Materials, 7 (2014) 5327-5355

[9] C.M. Ho, Y.C. Tai, Micro-electro-mechanical-systems (mems) and fluid flows, Annu. Rev. Fluid Mech., 30 (1998) 579-612.

[10] S.H. Kim, D.B. Asay, M.T. Dugger, Nanotribology and MEMS, Nano Today, 2 (2007) 22-29.

[11] S. Sathe, T.E. Tezduyar, Modeling of fluid-structure interactions with the space-time finite elements: contact problems, Comput. Mech., 43 (2008) 51-60.

[12] M. Cross, T.N. Croft, D. McBride, A.K. Slone, A.J. Williams, Multiphysics modelling and simulation: progress and challenges, Canada: NAFEMS World Congress (2007).

[13] E.H. Dowell, K.C. Hall, Modelling of Fluid-structure interaction, Annu. Rev. Fluid Mech. 33 (2001) 445-490.

[14] W. Wall, A. Gerstenberger, P. Gamnitzer, C. Forster, E. Ramm, Large deformation Fluid-Structure Interaction – Advances in ALE Methods and new fixed grid approaches, in: Bungartz H.J., Shafer M. (Eds.), Fluid-Structure Interaction, Springer-Verlag, Berlin, 2006.

[15] F.N. Van de Vosse, J. De Hart, C.H.G.A. Van Oijen, D. Bessems, T.W.M. Gunther, A. Segal, B.J.B.M. Wolters, J.M.A. Stijnen, F.P.T. Baaijens, Finite-element-based

computational methods for cardiovascular fluid-structure interaction, J. Eng. Math. 47 (2003) 335–368.

[16] J. Donea, An arbitrary Lagrangian–Eulerian Finite element method for transient fluid–structure interactions, Comput. Methods Appl. Mech. Eng. 33 (1982) 689 – 723.

[17] L. Formaggia, F. Nobile, A stability analysis for the arbitrary Lagrangian Eulerian formulation with finite elements, East–West J. Numer. Math. 7 (1999) 105 –132.

[18] H.Y.H Chen, T.W.H. Sheu, Finite-element simulation of incompressible fluid flow in an elastic vessel, Int. J. Numer. Meth. Fluids 42 (2003) 131–146.

[19] Comsol Users Manual, Comsol Multiphysics Users Guide, Comsol Ltd. London, 2005.

[20] M. Al Atabi, D.M. Espino, D.W.L. Hukins, K.G. Buchan, Biomechanical assessment of surgical repair of the mitral valve, Proc. Inst. Mech. Eng. H, 226 (2012) 275-287.

[21] C.G. Caro, T.J. Pedley, R.C. Schroter, W.A. Seed, The Mechanics of the Circulation, Oxford University Press, Oxford, 1978.

[22] C. Pozrikidis, Introduction to Finite and Spectral Element Methods Using MATLAB, Chapman & Hall/CRC, Boca Raton, 2005.

[23] J.F. Wendt, Computational Fluid Dynamics: An Introduction, Springer-Verlag, Berlin, 1992.

[24] S. Post, Applied and Computational Fluid Mechanics, Jones and Bartlett, Massachusetts, 2011.

[25] M.D. Gunzburger, Navier-Stokes equations for incompressible flows: finite-element methods, In: Peyret R. (Ed.), Handbook of Computational Fluid Mechanics, Academic Press, London, 1996.

[26] R.L. Lee, P.M. Gresho, R.L. Sani, Smoothing techniques for certain primitive variable solutions of the Navier-Stokes equations, Int. J. Numer. Meth. Eng. 14 (2005) 1785-1804.

[27] S. Turek, Lecture notes in Computational Science and Engineering, 6, Efficient Solvers for Incompressible Flow Problems: An Algorithmic Approach in View of Computational Aspects, Springer-Verlag, Heidelberg, 1999.

[28] M. Brewer, Obtaining smooth mesh transitions using vertex optimization, Int. J. Numer. Meth. Eng. 75 (2008) 555–576.

[29] R.A. Granger, Fluid Mechanics, Holt, Rinehart and Winston, New York, 1985.

[30] C.S. Peskin, Numerical analysis of blood flow in the heart, J. Comput. Phys. 25 (1977) 220–252.

[31] C.S. Peskin, Flow patterns around heart valves: A numerical method, J. Comput. Phys. 10 (1972) 252–270.

[32] F.P.T Baaijens, A fictitious domain/mortar element method for fluid–structure interaction, Int. J. Numer. Meth. Fluids 35 (2001) 743–761.

[33] J.M.A Stijnen, J. De Hart, P.H.M. Bovendeerd, F.N. Van de Vosse, Evaluation of a fictitious domain method for predicting dynamic response of mechanical heart valves, J. Fluid Struct. 19 (2004) 835-850.

[34] C.S. Peskin, The immersed boundary method, Acta Numer. 11 (2002) 479–517.

[35] D.M. Espino, D.E.T. Shepherd, K.G. Buchan, Effect of mitral valve geometry on valve competence, Heart Vessels 22 (2007) 109-115.

[36] D.M. Espino, D.E.T Shepherd, D.W.L. Hukins, K.G. Buchan, The role of chordae tendineae in mitral valve competence, J. Heart Valve Dis. 14 (2005) 603-609.

FIGURES CAPTIONS

Figure 1. Geometry, boundary conditions and mesh for simulations. (a) On the larger rectangles (i.e. conduits): red boundaries denote the application of pressure, green boundaries the fluid velocity, and blue boundaries a no-slip condition; on the smaller rectangle (deformable structure, i.e. leaflets): the shorter blue sides with a red-line denote a fixed boundary, while the blue boundary denotes the application of contact conditions; FSI occurs through the shared black boundary (i.e. use of velocity constraints and Lagrange multipliers). (b) Mesh used for FSI simulations. Scales are in metres. The deformable rectangle to the left is referred to as the anterior, and to the right the posterior, leaflet. Note, The solid domain is formed by AL (anterior leaflet) and PL (posterior leaflet); while, the fluid domain (FD) is contained within the conduits (i.e. larger rectangles within which fluid flow will occur). (c) Illustration of the heart, focusing on the left side of the heart which contains the mitral valve, surrounded by blood.

Figure 2. Comparison of a transient FSI analysis between the default (a, c, & d) and the new contact method (b, d, f) at time-steps of 1, 5 and 10 s.

Figure 3. Contact pressure distribution along the contacting boundary of the anterior leaflet at 10 s. (a) default and (b) new contact method (PB refers to contact pressure, in Pascals).

TABLES

Table 1. Material properties for structures and fluid used for simulations.

Anterior Leaflet Young's modulus (Pa)	Posterior Leaflet Young's modulus (Pa)	Poisson's ratio	Fluid density (Kg/m^3)	Viscosity (Pa.s)
5.00×10^6	2.00×10^6	0.33	1060	5.00×10^3

Table 2. Settings for solving simulations for both the default and new contact methods.

Contact method	Solution type	Total degrees of freedom solved	Number of Elements	Lagrange element type	BDF Max.
Default	Parametric	2820	290	Quadratic	n/a
New	Transient	2789	290	P2P1	4

BDF: backward differentiation formula [25].

P2P1: 2nd order (i.e. quadratic) Lagrange elements determine velocity (P2), while 1st order (i.e. linear) Lagrange elements determine the pressure (P1).

Table 3. Maximum and minimum values for stress, strain and contact pressure under a given loading pressure, per time step. Results are presented for both the default and new contact methods. Contact pressures are reported as zero when the computed values were less than 10^{-10} Pa.

	Time (s)		Pressure (kPa)	von Mises (Pa)	Cauchy stress (Pa)				Green strain			Contact pressure (Pa)
					σ_x	σ_y	σ_z	σ_{xy}	ε_x	ε_y	ε_{xy}	
a	1	max	1.70	2.40×10^5	1.20×10^5	2.95×10^5	1.20×10^5	3.30×10^4	0.03	0.09	0.017	0
		min	1.70	4.80×10^2	-9.90×10^4	-1.98×10^5	-9.90×10^4	-3.30×10^4	-0.04	-0.07	-0.017	0
b	1	max	1.70	2.10×10^5	1.00×10^5	2.50×10^5	1.00×10^5	2.70×10^4	0.03	0.08	0.015	6.72×10^3
		min	1.70	1.30×10^3	-8.90×10^4	-1.80×10^5	-8.90×10^4	-2.70×10^4	-0.03	-0.06	-0.015	0
a	5	max	8.10	7.60×10^5	3.00×10^5	8.80×10^5	2.30×10^5	1.80×10^5	0.09	0.24	0.050	1.70×10^4
		min	8.00	4.50×10^3	-2.50×10^5	-4.50×10^5	-2.50×10^5	-1.80×10^5	-0.10	-0.17	-0.050	-0.73×10^3
b	5	max	8.10	4.40×10^5	1.90×10^5	5.50×10^5	1.90×10^5	9.30×10^4	0.07	0.16	0.040	1.60×10^4
		min	8.00	3.20×10^3	-1.80×10^5	-3.60×10^5	-1.80×10^6	-9.40×10^4	-0.07	-0.14	-0.040	0
a	10	max	16.2	1.10×10^6	3.90×10^5	1.20×10^6	3.70×10^5	3.50×10^5	0.12	0.32	-0.080	2.50×10^4
		min	15.8	2.60×10^3	-3.50×10^5	-6.00×10^5	-3.50×10^5	-3.50×10^5	-0.13	-0.24	0.080	-1.30×10^3
b	10	max	16.2	6.50×10^5	2.40×10^5	7.10×10^5	2.40×10^5	1.80×10^5	0.10	0.20	0.060	2.90×10^4
		min	15.8	6.50×10^3	-2.50×10^5	-4.80×10^5	-2.50×10^5	-1.80×10^5	-0.10	-0.20	-0.060	0

a. default contact method;

b. new contact method.

Table 4. Maximum and minimum values for flow parameters per given time step, including the *x-axis* and *y-axis* Lagrange multipliers (λ_5 and λ_6, respectively). Results are presented for both the default and new contact methods. Velocities (in m/s) and cell Reynolds numbers are reported as zero when the computed values were less than 10^{-10}.

	time (s)		Pressure (kPa)	*x-velocity* (m/s)	*y-velocity* (m/s)	velocity field (m/s)	Vorticity (1/s)	cell Reynold's number	λ_5	λ_6
a	1	max	1.70	0.013	0.204	0.204	0.21×10^{3}	0.21×10^{3}	1.70×10^{3}	0.38×10^{3}
		min	1.70	-0.010	-0.014	0	-0.18×10^{3}	0	-1.70×10^{3}	-0.38×10^{3}
b	1	max	1.70	0.013	0.200	0.200	0.22×10^{3}	0.21×10^{3}	1.70×10^{3}	0.35×10^{3}
		min	1.70	-0.011	-0.014	0	-0.19×10^{3}	0	-1.70×10^{3}	-0.35×10^{3}
a	5	max	8.10	0.044	1.020	1.020	1.35×10^{3}	1.10×10^{3}	8.10×10^{3}	3.30×10^{3}
		min	8.00	-0.034	-0.070	0	-0.86×10^{3}	0	-8.10×10^{3}	-3.30×10^{3}
b	5	max	8.10	0.045	1.020	1.020	1.26×10^{3}	1.08×10^{3}	8.10×10^{3}	2.50×10^{3}
		min	8.00	-0.035	-0.070	0	-0.89×10^{3}	0	-8.10×10^{3}	-2.50×10^{3}
a	10	max	16.2	0.078	2.060	2.060	2.90×10^{3}	2.27×10^{3}	1.60×10^{4}	7.80×10^{3}
		min	15.8	-0.074	-0.180	0	-1.60×10^{3}	0	-1.60×10^{4}	-7.80×10^{3}
b	10	max	16.2	0.080	2.060	2.060	2.60×10^{3}	2.16×10^{3}	1.62×10^{4}	5.80×10^{3}
		min	15.8	-0.080	-0.140	0	-1.70×10^{3}	0	-1.58×10^{4}	-5.70×10^{3}

a. default contact method;

b. new contact method.

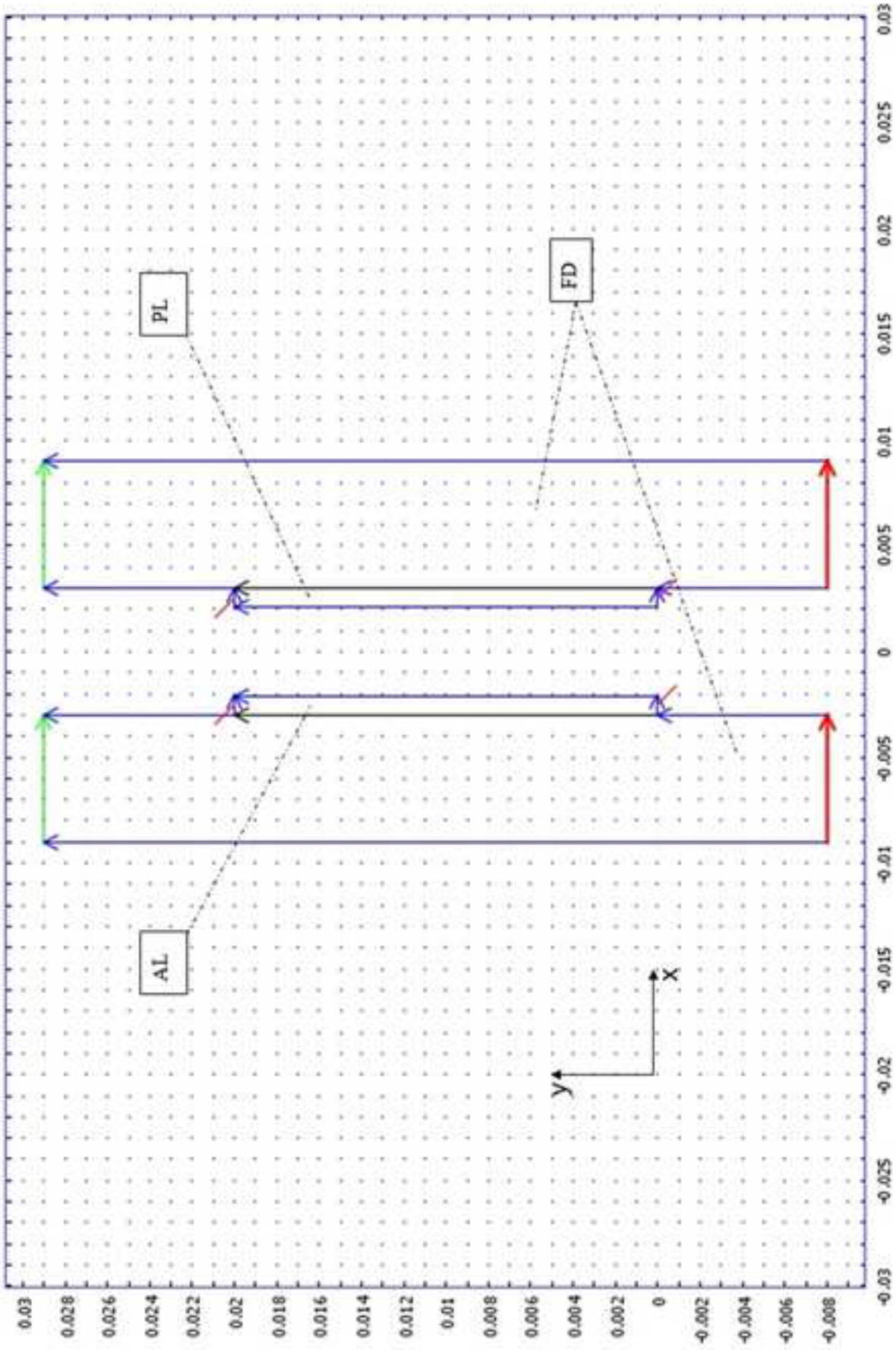

Figure 1a
Click here to download high resolution image

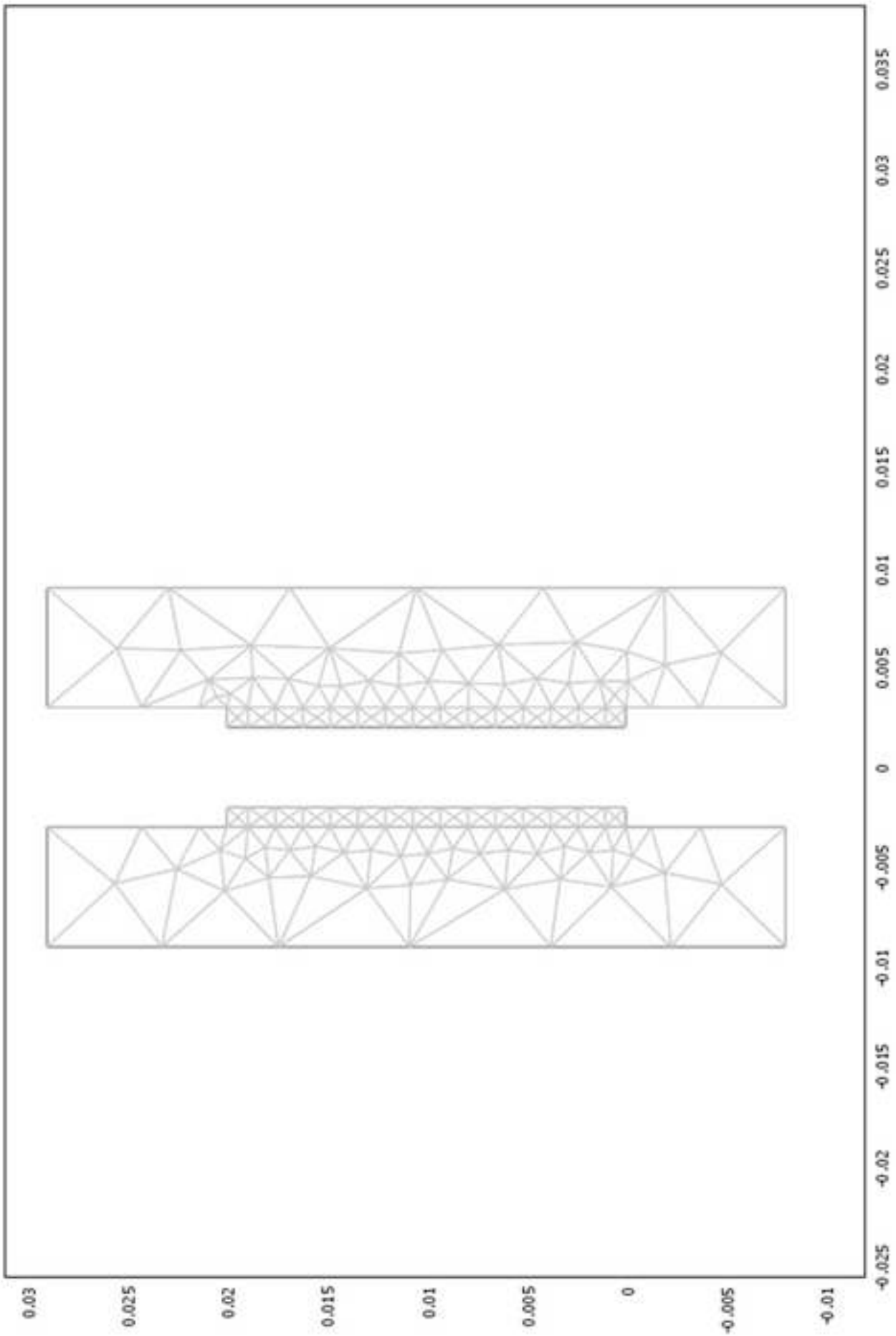

Figure 1b
Click here to download high resolution image

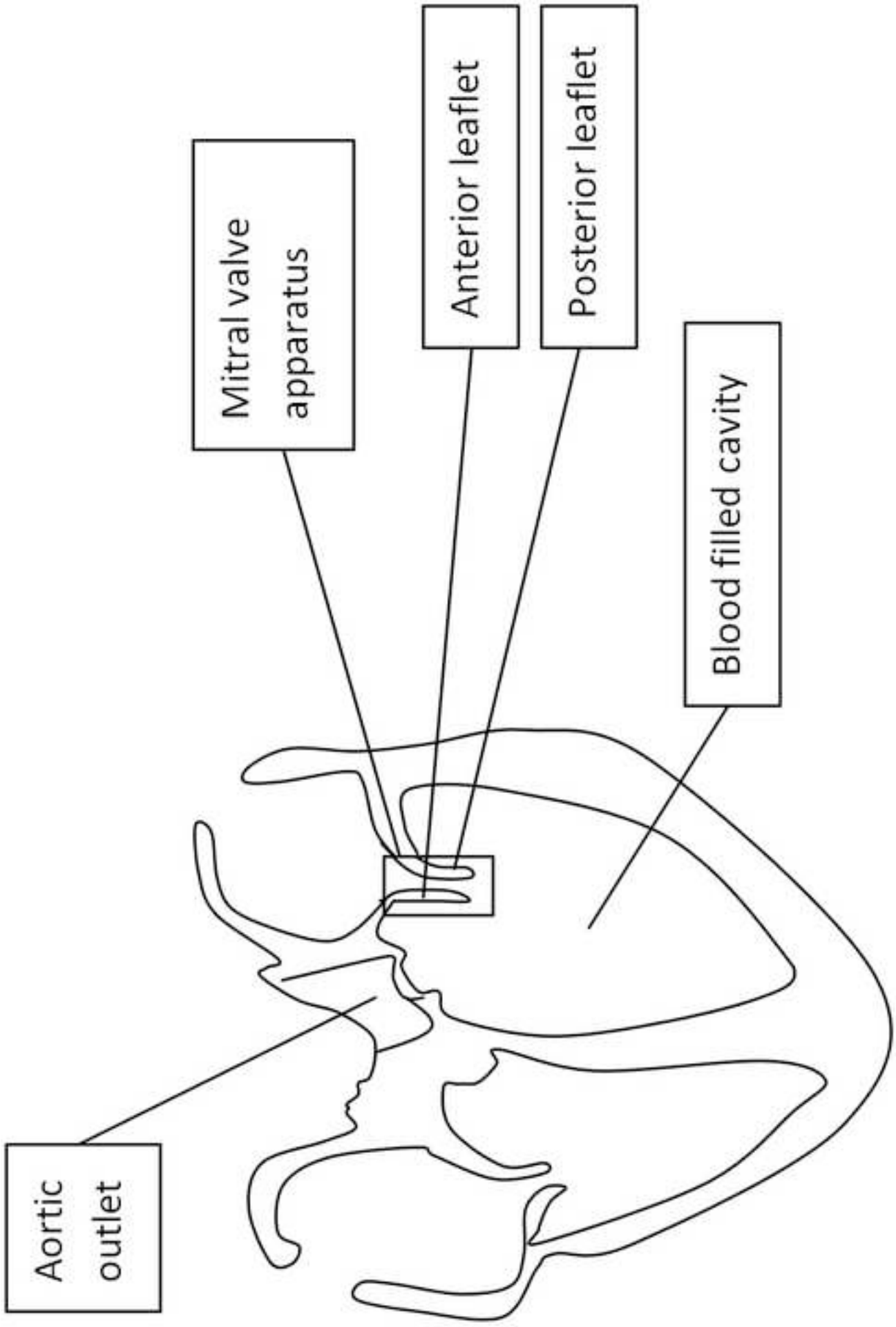

Figure 1c
Click here to download high resolution image

Figure 2a

Click here to download high resolution image

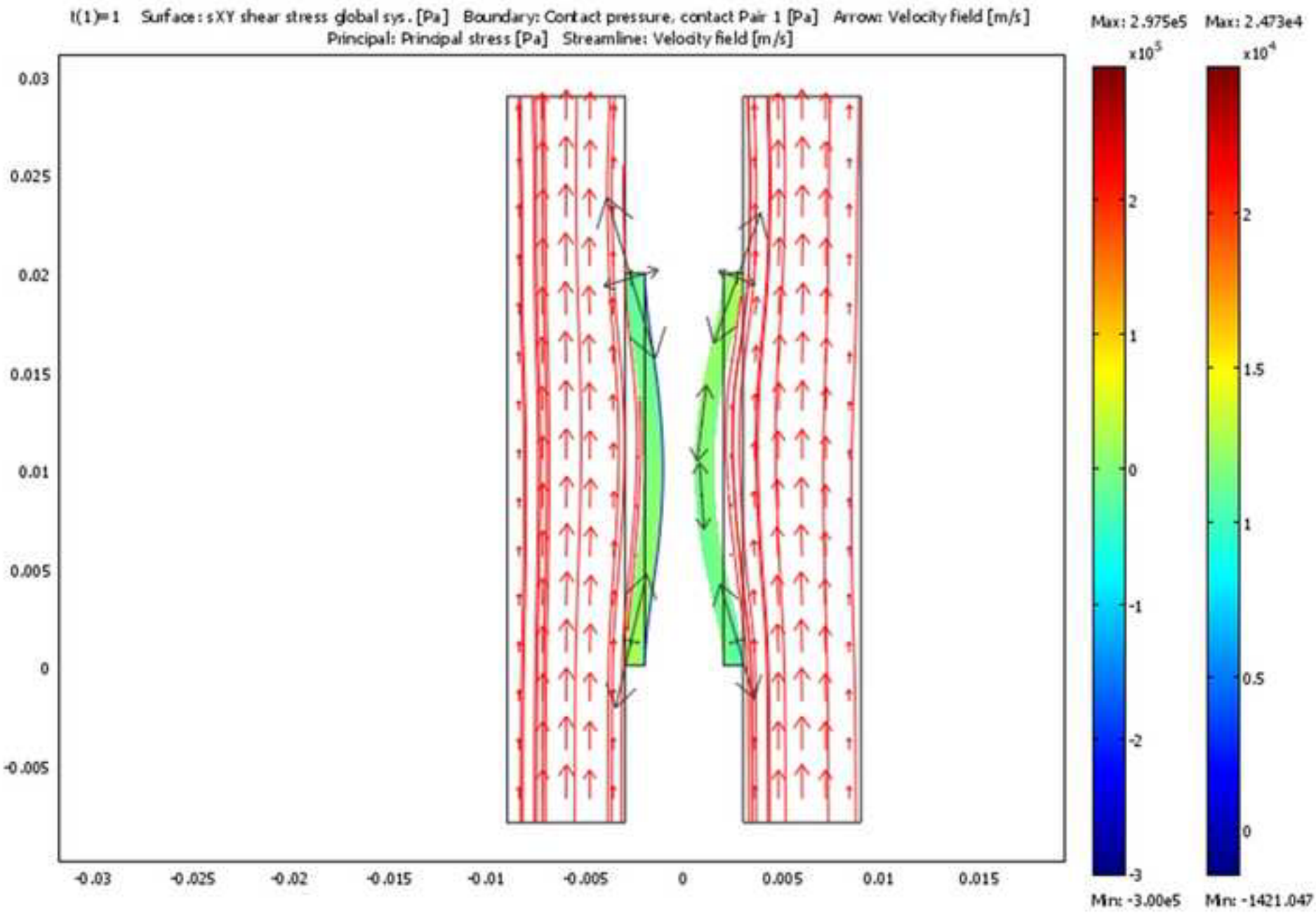

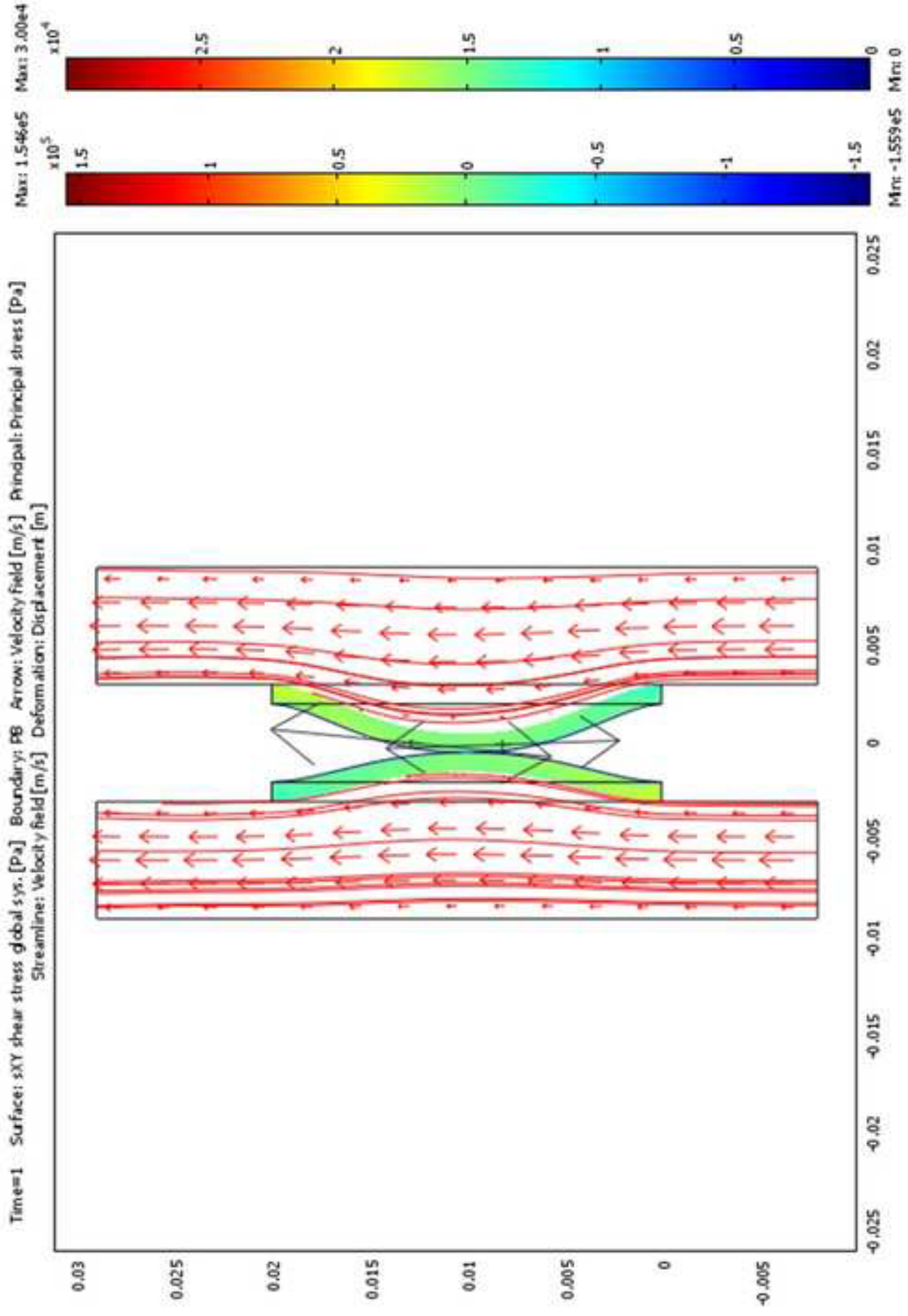

Figure 2b
Click here to download high resolution image

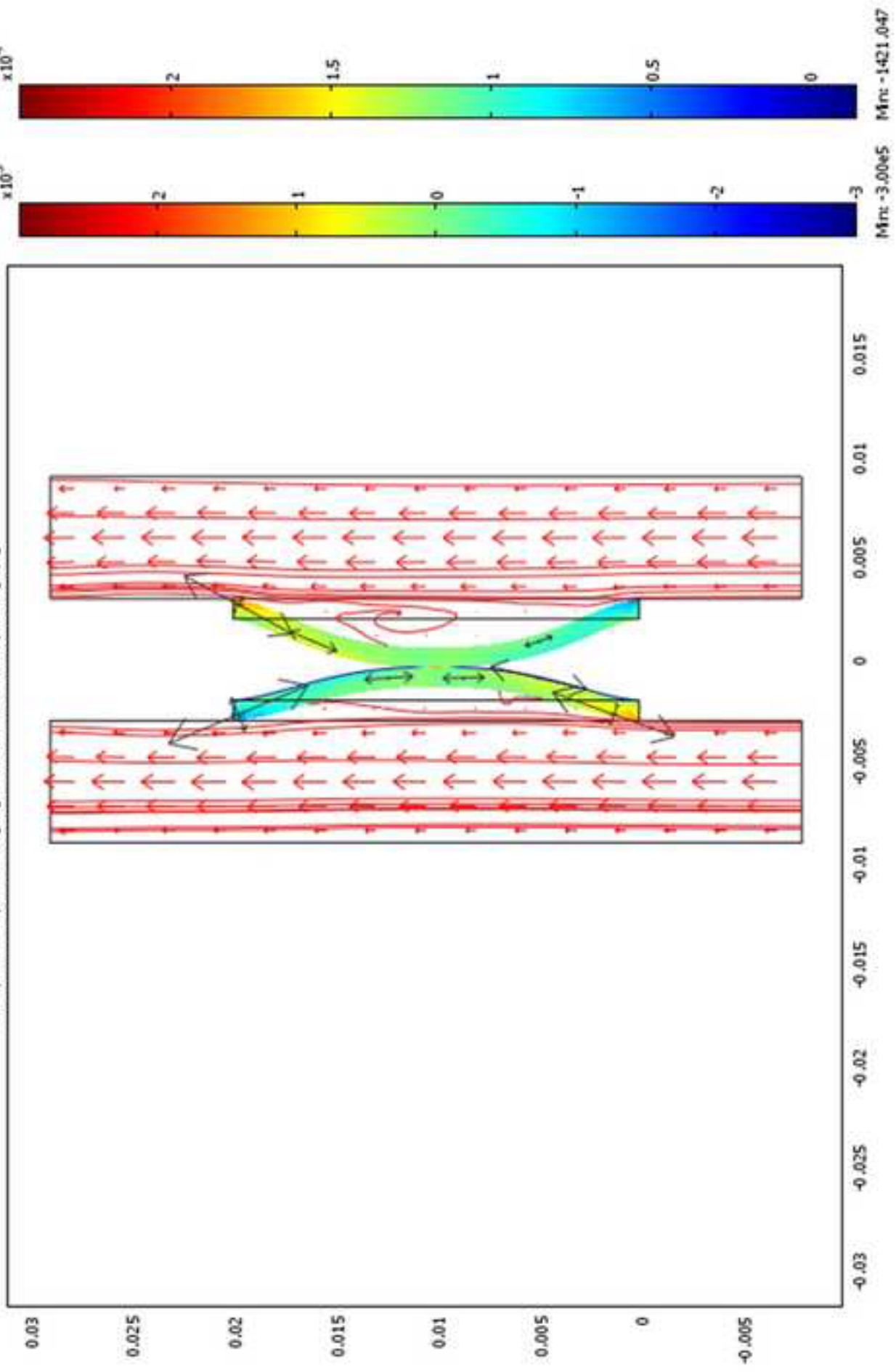

Figure 2c
Click here to download high resolution image

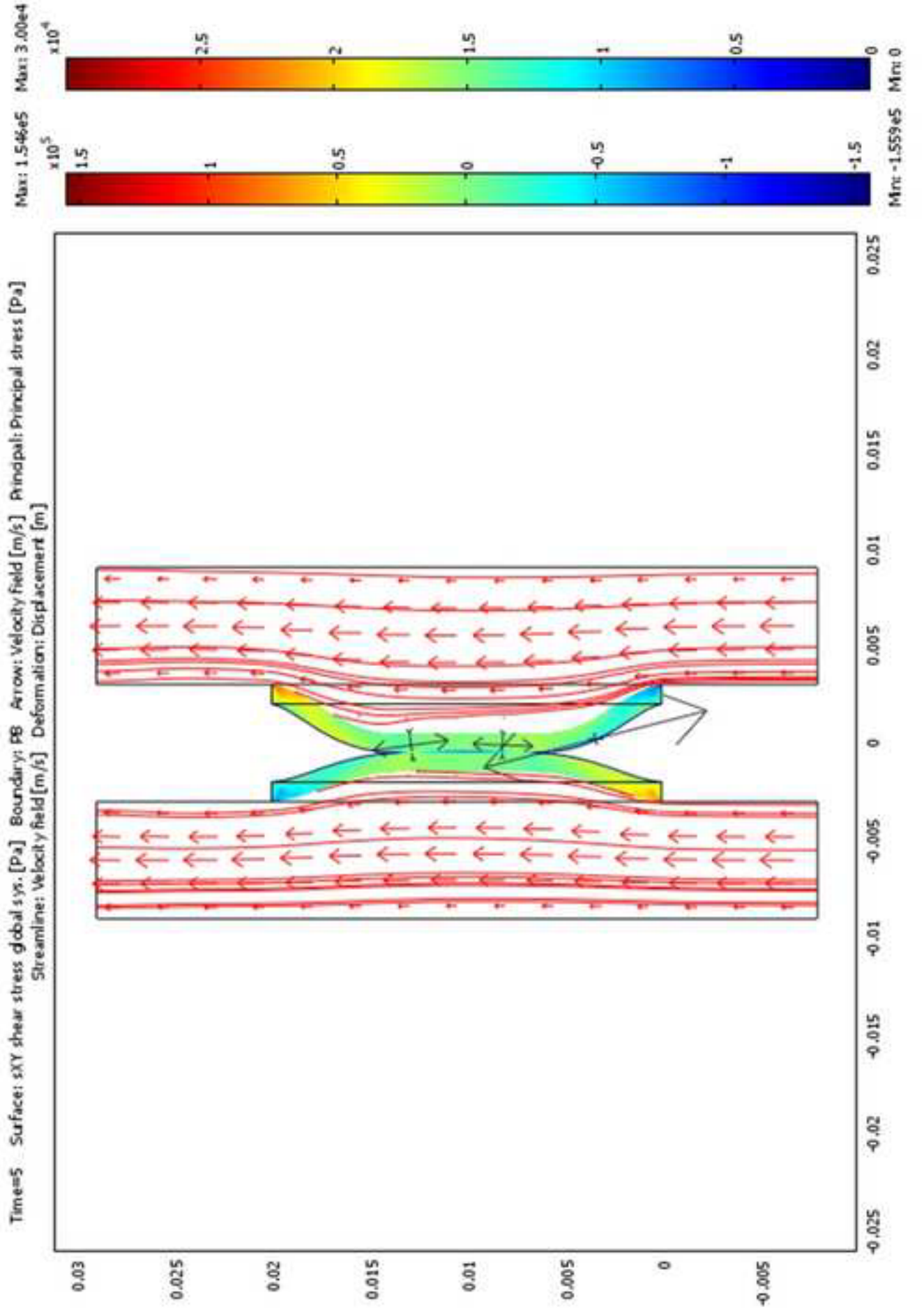

Figure 2d
Click here to download high resolution image

Figure 2e

Click here to download high resolution image

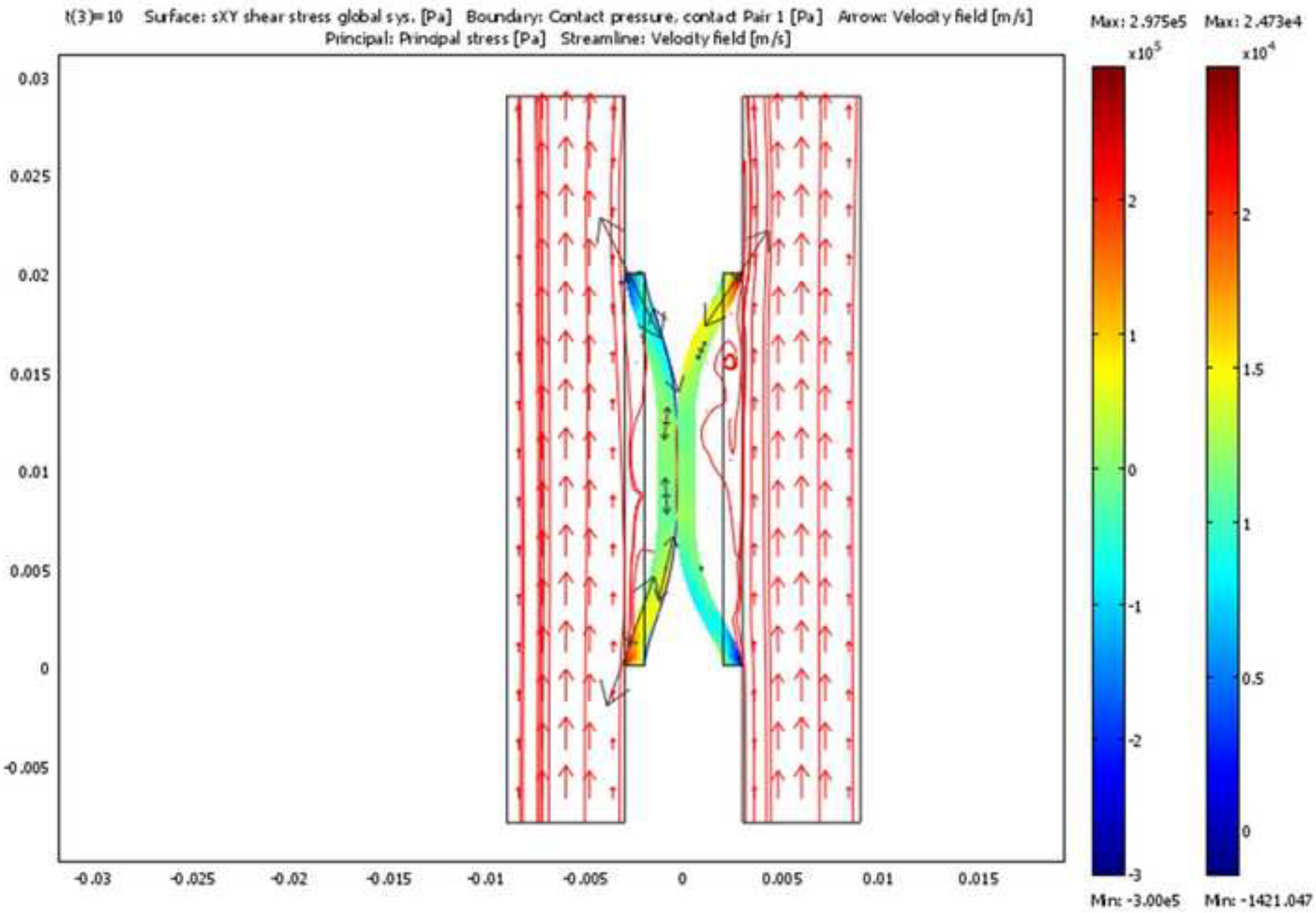

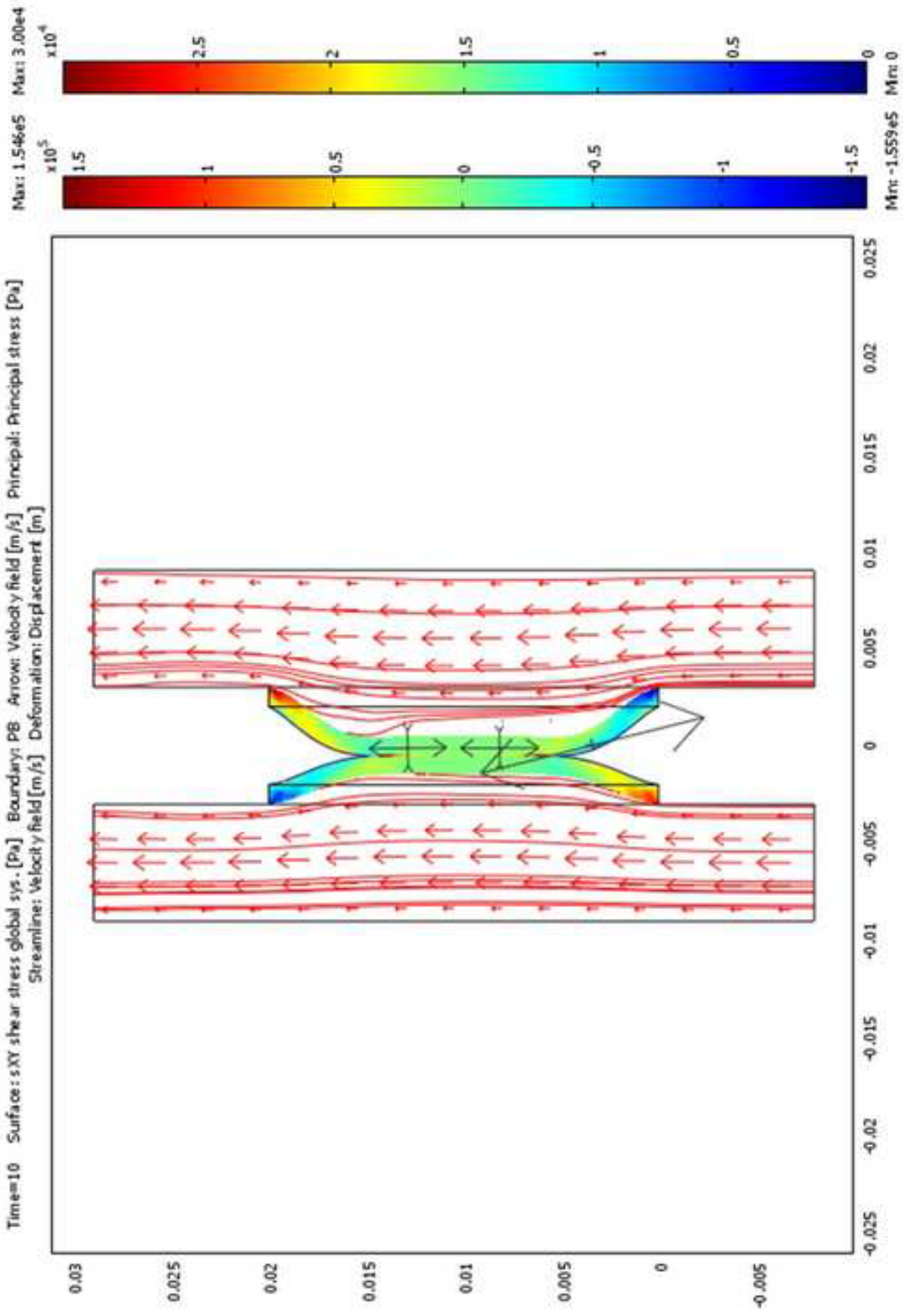

Figure 2f
Click here to download high resolution image

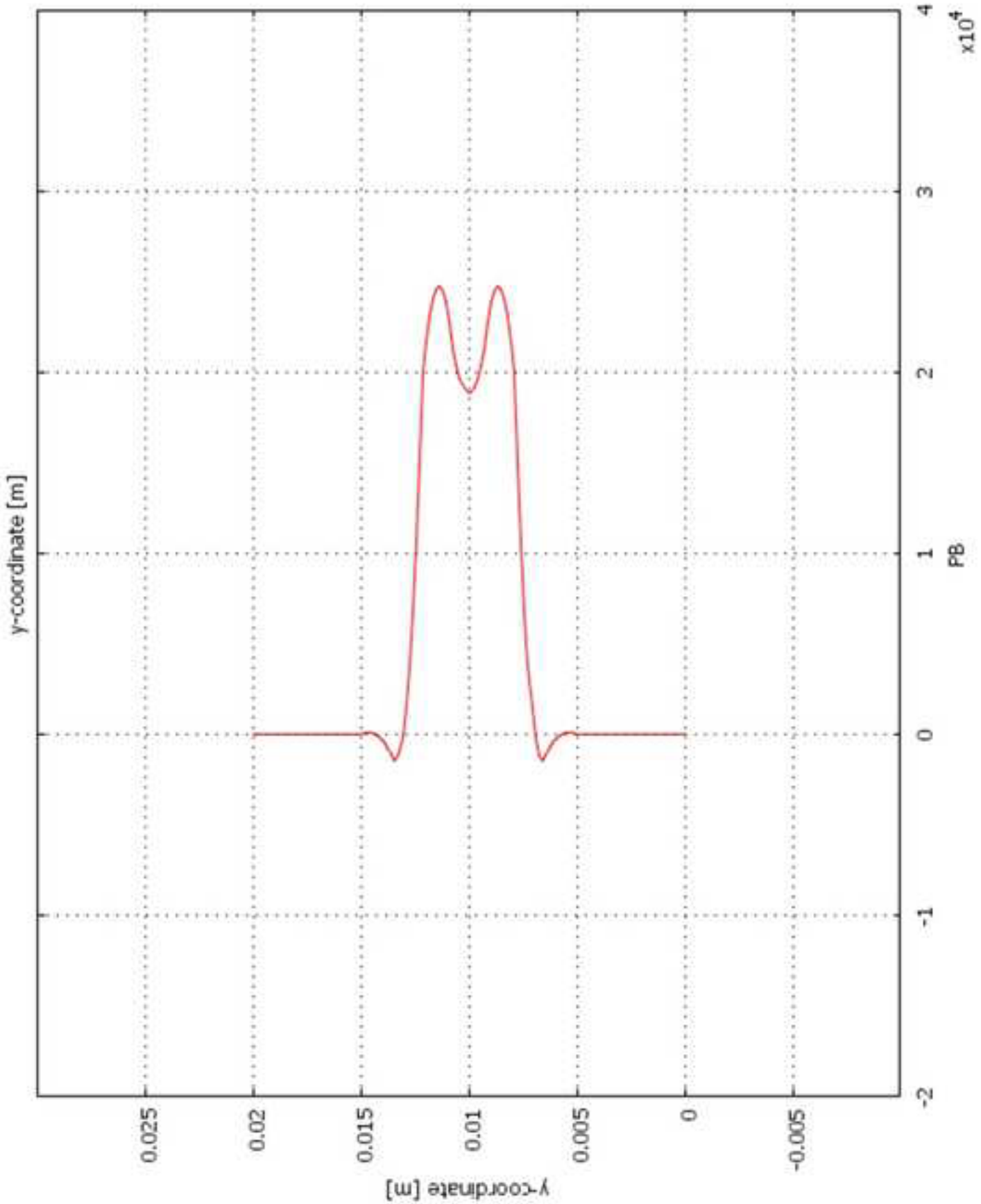

Figure 3a
Click here to download high resolution image

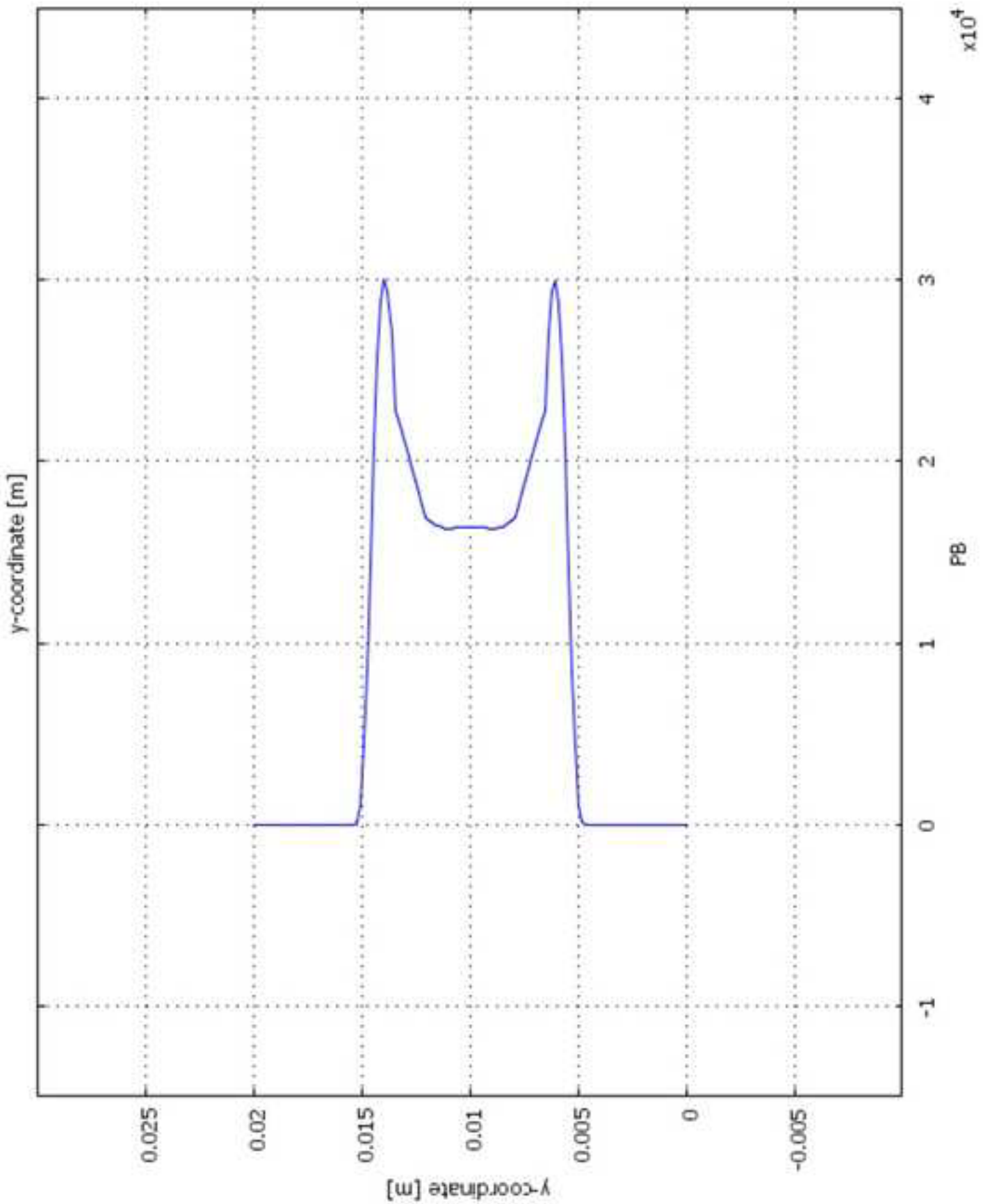

Figure 3b
Click here to download high resolution image